Preprints (www.preprints.org) | NOT PEER-REVIEWED | Posted: 5 March 2021 doi:10.20944/preprints202103.0206.v1

Article

Predicting electrokinetic coupling and electrical conductivity in fractured media using a bundle of tortuous capillary fractures

Luong Duy Thanh [1,†], Damien Jougnot [2,†,*], Phan Van Do [1], Dang Thi Minh Hue [1], Tran Thi Chung Thuy [1] and Vu Phi Tuyen [3]

[1] Thuyloi University, 175 Tay Son, Dong Da, Hanoi, Vietnam
[2] Sorbonne Université, CNRS, EPHE, UMR 7619 Metis, F-75005, Paris, France
[3] National Institute of Information and Communications Strategy - MIC, Hanoi, Vietnam
* Correspondence: damien.jougnot@upmc.fr
† These authors contributed equally to this work.

Abstract: The electrokinetics methods have a great potential to characterize hydrogeological processes in geological media, especially in complex hydrosystems such as fractured formations. In this work, we conceptualize fractured media as a bunch of parallel capillary fractures following the fractal size distribution. This conceptualization permits to obtain analytical models for both the electrical conductivity and the electrokinetic coupling in water saturated fractured media. We explore two different approaches to express the electrokinetic coupling. First, we express the streaming potential coupling coefficient as a function of the zeta potential and then we obtain the effective charge density in terms of macroscopic hydraulic and electrokinetic parameters of porous media. We show that when the surface electrical conductivity is negligible, the proposed models reduces to the previously proposed one based on a bundle of cylindrical capillaries. This model opens up a wide range of applications to monitor the water flow in fractured media.

Keywords: Fractured media; Streaming potential; Electrical conductivity; Fractal

1. Introduction

Among many geophysical methods, electrical conductivity imaging and streaming potential (SP) measurements attract an increasing interest to better understand and monitor water distribution and dynamics in hydrosystems, aquifers, or reservoirs [e.g., 1–3]. These geo-electrical methods are used to detect and monitor groundwater flow [e.g., 4–9], geothermal areas and volcanoes [e.g., 10–12], detection of contaminant plumes [e.g., 13,14], monitoring water flow in the vadose zone [e.g., 9,15,16] or eco-hydrology [e.g., 17,18]. Thanks to accurate petrophysical relationships and advanced hydrogeophysical inversion approaches, these geo-electrical methods can be exploited to estimate hydrogeological parameters of the aquifer [e.g., 19,20]. Nevertheless, complex environments such as fractured media and karstic formations remain a challenge for geo-electrical methods.

Even if fractured media constitute a large fraction of hydrosystems, it remains largely under studied. The interest of geo-electrical methods to study fractured media is clearly established in the literature using electrical conductivity [e.g., 21–23] or streaming potential [e.g., 5,24,25], but the quantitative use of these methods remains scarce in the literature.

The nature of fractured media makes it a challenge for integrative methods such as electrical conductivity imaging and streaming potential [26]. Indeed, fractures usually present a huge contrast in terms of properties with the surrounding matrix making it difficult to be clearly identified through diffusion-based methods such as electrical resistivity tomography [e.g., 27,28]. Different numerical methods have been proven useful for both electrical conductivity and self-potential simulations, among which the very fine discretization in finite-element modelling [e.g., 29,30] or discrete-dual-porosity [e.g., 23,31]. Nevertheless, analytical models and petrophysical relationships can be beneficial to the development and use of geo-electrical methods through for faster and simpler approaches.

Petrophysical relationships relating electrical conductivity and structural properties in fractured media are not abundant in the literature. Among other works, Bernabe [32] uses

© 2021 by the author(s). Distributed under a Creative Commons CC BY license.

Preprints (www.preprints.org) | NOT PEER-REVIEWED | Posted: 5 March 2021 doi:10.20944/preprints202103.0206.v1

crack networks and percolation to study the transport properties, while Roubinet et al. [33] revisited the classic model of Archie [34] to relate topological and electrical properties. To the best of the authors knowledge, no analytical petrophysical relationships for fractured media exist in the literature.

Regarding the modeling of electrokinetic coupling, the most crucial parameter is the streaming potential coupling coefficient (SPCC). The SPCC controls the coupling between the fluid flow and the electrical field in porous media. It can be obtained through either the Helmholtz-Smoluchoski (HS) equation or the effective excess charge density approach. The HS equation is commonly used to determine the SPCC via the zeta potential at the solid liquid interface, fluid properties for a single cylindrical capillary [e.g., 35,36]. Applying a volume averaging procedure, Pride [37] showed that the HS equation is still valid for porous media as long as the surface conductivity can be neglected [see also, 38]. Modified HS equations have been proposed in the literature when the surface conductivity cannot be neglected [e.g., 39–41]. Then, an alternative approach allows the determination of the SPCC via the excess charge that is effectively dragged by the water flow in porous media [e.g., 42–44]. Capillary-based models have been successfully applied to describe SP in porous media, i.e., the porous medium is described as a bundle of parallel cylindrical tubes [e.g., 45–56]. However, microstructure of porous media is normally very complex with tortuous and non-circular pores. Recently, Shi et al. (2018) have theoretically studied the dependence of dynamic electrokinetic coupling coefficient on the electrical double layer thickness for a single cylindrical capillary and a single capillary fracture [57]. Then, they directly extended the obtained electrokinetic coupling coefficient from a single capillary to porous media without applying the upscaling technique. It should be noted that the electroosmosis that is a opposite effect to the SP in porous media has also been studied using capillary bundle models with different capillary geometry such as rectangular, cylindrical and annular geometries [e.g., 58–61]. Nevertheless, to the best of our knowledge, no model has been published to describe both the electrical conductivity an the electrokinetic coupling using a distribution of rectangular (i.e., fracture-like) capillaries.

Therefore, in this work, we conceptualize porous media as a bunch of tortuous parallel fractures or rectangular cross-sections following the fractal pore size distribution to study electrical conductivity and electrokinetic coupling in fractured media. Namely, we develop the model for the SPCC that is expressed in terms of both the zeta potential and the effective charge density. We also propose an analytical model for the effective charge density in terms of macroscopic hydraulic and electrokinetic parameters of porous media. Incidentally, we also obtain an expression for the electrical conductivity of saturated fractured media. All the proposed models are then compared with experimental data available in literature and published models.

2. Theory of the electrokinetic coupling

The streaming current is controlled by the relative movement between the charged solid surfaces and pore fluid and is directly related to an electric double layer (EDL) existing at the interface between the fluid and solid surfaces [e.g., 35]. This streaming current is then balanced out by a conduction current, leading to a so-called streaming potential. In other words, the water flowing through porous media creates a streaming potential [e.g., 62]. The important parameter for SP is the SPCC. At the steady state condition, the SPCC is defined as [e.g., 39]:

$$C_S = \frac{\Delta V}{\Delta P}, \tag{1}$$

where ΔV (V) and ΔP (Pa) are the generated streaming potential and applied fluid pressure difference, respectively. There normally exist two expressions to determine the SPCC at fully saturated conditions in literature. The first one is the HS equation that links the SPCC with the zeta potential ζ (V) at the solid-liquid interface and fluid properties and is given by [63]

$$C_S = \frac{\epsilon_r \epsilon_0 \zeta}{\eta \sigma_w}, \tag{2}$$

Preprints (www.preprints.org) | NOT PEER-REVIEWED | Posted: 5 March 2021 doi:10.20944/preprints202103.0206.v1

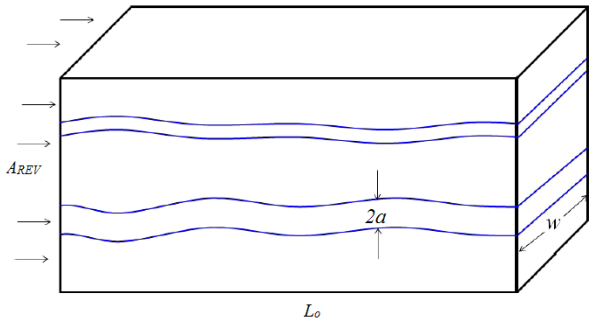

Figure 1. Schematic view of a fractured medium composed of a bunch of parallel slits.

where ϵ_r (no units) is the relative permittivity of the fluid, ϵ_0 (F/m) is the dielectric permittivity in vacuum, η (Pa s) is the dynamic viscosity and σ_w (S/m) is the electrical conductivity of the fluid. Eq. (2) is valid when the surface electrical conductivity of porous media is neglected [e.g., 38]. When the surface electrical conductivity is taken into account, one can apply the modified HS equation given by [e.g., 36,40,41]

$$C_S = \frac{\epsilon_r \epsilon_0 \zeta}{\eta(\sigma_w + 2\frac{\Sigma_s}{\Lambda})}, \tag{3}$$

where Σ_s (S) the specific surface conductance and Λ (m) is a characteristic length scale [64].

Addition to the HS equation or modified HS equation, the SPCC can be expressed via the effective excess charge density dragged by pore water in porous media as [e.g., 42–44]

$$C_S = -\frac{k\widehat{Q}_v}{\eta\sigma}. \tag{4}$$

where $\widehat{Q}_v$ (C/m^3), k (m^2) and σ (S/m) are the effective excess charge density, permeability and electrical conductivity of porous media at fully saturated conditions, respectively. Note that the electrical conductivity plays a very important role in the electrokinetic coupling.

3. Theoretical development

3.1. Geometry of fractured media

It has been shown that the fractal geometry can be applied in analysis of flow and transport properties in porous media in general and specifically in fractured media [e.g., 65–69]. Fractured media are assumed to be composed of the fractures and the surrounding matrix [e.g., 70]. The matrix permeability is normally much smaller than that of the fractures and thus the matrix can be considered as impermeable and no fluid exchange through the fracture walls. In this work, fractures are conceptualized as a bunch of parallel capillary slits as shown in Fig. 1. The fracture is approximately considered as plane with rectangular cross-section, whose widths follow the fractal scaling law [e.g., 71–73]. The aperture and width of parallel fractures are $2a$ (m) and w (m), respectively. In order to derive electrokinetic properties at macroscale, we consider a representative elementary volume (REV) as a cube with the length of L_o and the cross-section area of the REV perpendicular to the flow direction of A_{REV} (see Fig. 1). As mentioned, the REV is conceptualized as a bundle of fractures with width varying from w_{min} to w_{max}. It is shown that the number of fractures whose widths are in the range from w to $w + dw$ in the REV is given by [e.g., 72–75]:

$$-dN = D_f w_{max}^{D_f} w^{-D_f-1} dw, \tag{5}$$

where D_f (no units) is the fractal dimension for pore space, $0 < D_f < 2$ in two-dimensional space and $0 < D_f < 3$ in three dimensional space. The negative sign in Eq. (5) implies that the number of fractures decreases with an increase of fracture width. The fractal

Preprints (www.preprints.org) | NOT PEER-REVIEWED | Posted: 5 March 2021 doi:10.20944/preprints202103.0206.v1

dimension for fracture space (D_f) can be estimated from properties of porous media using the following relation [e.g., 72,73]

$$D_f = 2 - \frac{\ln\phi}{\ln\alpha}, \tag{6}$$

where ϕ is the porosity of porous media and α is the ratio of the minimum width to the maximum width of the fractures ($\alpha = w_{min}/w_{max}$).

It has been shown that the aperture a (m) is related to the width w (m) of the fracture by the following linear scaling law [e.g., 72,73,76,77]:

$$a = \beta w, \tag{7}$$

where β is the fracture aspect ratio.

3.2. Hydraulic properties

The porosity of the REV defined above can be computed as the ratio of the total pore volume V_p and the total volume V_{REV} of the REV:

$$\begin{aligned}\phi = \frac{V_p}{V_{REV}} &= \frac{\int_{w_{min}}^{w_{max}}(2aw)(L_\tau)(-dN)}{L_o A_{REV}} = \frac{2\beta\tau D_f w_{max}^{D_f}}{A_{REV}}\int_{w_{min}}^{w_{max}} w^{1-D_f}dw \\ &= \frac{2\beta\tau D_f w_{max}^2}{A_{REV}(2-D_f)}(1-\alpha^{2-D_f}),\end{aligned} \tag{8}$$

where L_o is the length of the REV, L_τ is the real length of the fracture and τ=L_τ/L_o is the dimensionless hydraulic tortuosity of the microfracture [e.g., 78]. For the sake of simplicity, the length of the fractures is assumed to be independent of the fracture width, so an average tortuosity τ is considered in the model. It is trivial to take into account the correlation between the tortuosity and the capillary size as performed by [69,79,80], for example. However, this extra complexity does not really make the model any more representative of real porous media or affect the key results of the model [e.g., 46].

For a laminar flow, the velocity profile and average velocity (see Fig. 2) inside the fracture are, respectively, given by [e.g., 57,81]

$$v(y) = \frac{a^2}{2\eta}\left[1-\frac{y^2}{a^2}\right]\frac{\Delta P}{L_\tau} = \frac{a^2}{2\eta\tau}\left[1-\frac{y^2}{a^2}\right]\frac{\Delta P}{L_o}, \tag{9}$$

and

$$v_{av} = \frac{a^2}{3\eta\tau}\frac{\Delta P}{L_o}, \tag{10}$$

where ΔP is the fluid pressure difference, η is the dynamic viscosity of the fluid, a is the half aperture and y is the coordinate along the aperture as shown in Fig. 2.

The flow rate through a fracture is therefore given by

$$q = v_{av}.(2aw) = \frac{2a^3 w}{3\eta\tau}\frac{\Delta P}{L_o}. \tag{11}$$

It is noted that Eq. (11) is the well-known cubic law [e.g., 82,83]

Consequently, the total volumetric flow through the REV is the sum of volumetric flow rates through all fractures and is given by:

$$V_{REV} = \int_{w_{min}}^{w_{max}} q(-dN). \tag{12}$$

Combining Eq. (5), Eq. (7), Eq. (11) and Eq. (12) yields:

Preprints (www.preprints.org) | NOT PEER-REVIEWED | Posted: 5 March 2021 doi:10.20944/preprints202103.0206.v1

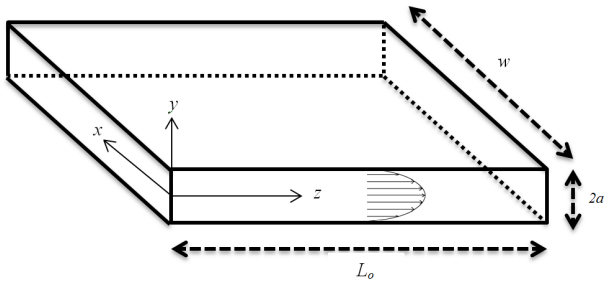

Figure 2. Fluid flow in a fracture and the coordinate along the aperture ($a << w << L_o$).

$$V_{REV} = \int_{w_{min}}^{w_{max}} \frac{a^2}{3\eta\tau}\frac{\Delta P}{L_o}(2aw)[D_f w_{max}^{D_f} w^{-D_f-1} dw] = \frac{2}{3\eta\tau} D_f \beta^3 w_{max}^4 \frac{1-\alpha^{4-D_f}}{4-D_f}\frac{\Delta P}{L_o}. \tag{13}$$

According to Darcy's law (macroscopic scale) for Newtonian fluid flow in porous media, V_{REV} is expressed as

$$V_{REV} = \frac{kA_{REV}}{\eta}\frac{\Delta P}{L_o}. \tag{14}$$

Combining Eq. (8), Eq. (13) and Eq. (14), the following is obtained

$$k = \frac{\beta^2 w_{max}^2 \phi}{3\tau^2}\frac{1-\alpha^{4-D_f}}{4-D_f}\frac{2-D_f}{1-\alpha^{2-D_f}}. \tag{15}$$

In case of $w_{max} >> w_{min}$ ($\alpha \to 0$), Eq. (15) reduces to

$$k = \frac{\beta^2 w_{max}^2 \phi}{3\tau^2}\frac{2-D_f}{4-D_f}. \tag{16}$$

3.3. Electrical conductivity

Adapting the reported approach for the electrical conductivity in porous media [e.g., 46,84], the bulk conductivity within a single fracture is given by

$$\sigma_{fb} = \sigma_w \frac{2aw}{A_{REV}\tau} = \sigma_w \frac{2\beta w^2}{A_{REV}\tau}. \tag{17}$$

The surface conductivity within a single fracture is given by

$$\sigma_{fs} = \Sigma_s \frac{2w+4a}{A_{REV}\tau} = \Sigma_s \frac{2(1+2\beta)w}{A_{REV}\tau}, \tag{18}$$

recall that $2aw$ and $2w+4a$ are the cross sectional area and the perimeter of the fracture (see Fig. 1). Consequently, the total electrical conductivity in a fracture is given by

$$\sigma_f(w) = \sigma_{fb} + \sigma_{fs} = \sigma_w \frac{2\beta w^2}{A_{REV}\tau} + \Sigma_s \frac{2(1+2\beta)w}{A_{REV}\tau}. \tag{19}$$

The electrical conductivity of the REV σ under saturated conditions is obtained by integrating over all saturated capillaries as

$$\sigma = \int_{w_{min}}^{w_{max}} \sigma_f(w)(-dN). \tag{20}$$

Combining Eq. (5), Eq. (19) and Eq. (20), the following is obtained

Preprints (www.preprints.org) | NOT PEER-REVIEWED | Posted: 5 March 2021 doi:10.20944/preprints202103.0206.v1

$$\sigma = \frac{1}{A_{REV}\tau}\left\{2\sigma_w\beta D_f w_{max}^2\frac{1-\alpha^{2-D_f}}{2-D_f} + 2\Sigma_s(1+2\beta)D_f w_{max}\frac{1-\alpha^{1-D_f}}{1-D_f}\right\}.$$
$$= \frac{2\beta D_f w_{max}^2(1-\alpha^{2-D_f})}{A_{REV}(2-D_f)\tau}\left\{\sigma_w + \frac{(1+2\beta)\Sigma_s}{\beta w_{max}}\frac{2-D_f}{1-D_f}\frac{1-\alpha^{1-D_f}}{1-\alpha^{2-D_f}}\right\}. \quad (21)$$

Substituting A_{REV} from Eq. (8) into Eq. (21), the electrical conductivity of porous media σ under saturated conditions is obtained as

$$\sigma = \frac{\phi}{\tau^2}\left\{\sigma_w + \frac{(1+2\beta)\Sigma_s}{\beta w_{max}}\frac{2-D_f}{1-D_f}\frac{1-\alpha^{1-D_f}}{1-\alpha^{2-D_f}}\right\}. \quad (22)$$

Eq. (22) indicates that the electrical conductivity of fractured media under saturated conditions is explicitly related to the porosity, electrical conductivity of the pore liquid, specific surface conductance and microstructural parameters of porous media (D_f, ϕ, α, β, w_{max}). It has the similar form to published models for porous media [e.g., 37,85–90]. From Eq. (22), the formation factor F is deduced as [34]:

$$F = \lim_{\Sigma_s \to 0}\left(\frac{\sigma_w}{\sigma}\right) = \frac{\tau^2}{\phi}. \quad (23)$$

Roubinet et al. (2018) conducted a systematic numerical analysis for modeling electrical current flow in complex and heterogeneous fractured rocks [33]. For simple case of a simple fracture–matrix system with N_f horizontal fractures embedded in a matrix having domain size L ($\tau = 1$), fracture aperture b_f and matrix porosity ϕ_b, the formation factor of such a domain is given by [33]

$$F = \frac{L}{\left[N_f b_f + (L - N_f b_f)\phi_b^{m_b}\right]}, \quad (24)$$

where m_b is the cementation factor for the matrix. If a matrix is impervious to electrical current, that is, $\phi_b = 0$, for which the porosity only depends on the fractures as $\phi = N_f b_f / L$, Eq. (24) now becomes for fractured media $F = \phi^{-1}$. This is expected from simple geometry principles, as for parallel straight and horizontal capillaries with no surface conductivity: $\sigma = \phi\sigma_w$.

Eq. (22) can be rewritten as:

$$\sigma = \frac{1}{F}\left\{\sigma_w + \frac{(1+2\beta)\Sigma_s}{\beta w_{max}}\frac{2-D_f}{1-D_f}\frac{1-\alpha^{1-D_f}}{1-\alpha^{2-D_f}}\right\}. \quad (25)$$

3.4. Streaming potential coupling coefficient

3.4.1. Streaming current in the REV

Adapting the strategy given by [91], the streaming current in a fracture due to transport of charge by the fluid under a fluid pressure difference is given by

$$i_s(a) = \int_{-a}^{+a} v(y)\bar{Q}_v(y)(w.dy), \quad (26)$$

where a is the half aperture and y is the coordinate along the aperture as shown in Fig. 2, $v(y)$ (m/s) is the velocity profile given by Eq. (9) and $\bar{Q}_v(y)$ (C/m^3) is the charge distribution in a fracture. Under Debye-Hückel approximation and the fluid of a binary symmetric 1:1 electrolyte [e.g., 51,92], $\bar{Q}_v(y)$ is given by [e.g., 57,93]

$$\bar{Q}_v(y) = -\frac{\epsilon_r\epsilon_o\zeta}{\lambda^2}\frac{\cosh(\frac{y}{\lambda})}{\cosh(\frac{a}{\lambda})}, \quad (27)$$

Preprints (www.preprints.org) | NOT PEER-REVIEWED | Posted: 5 March 2021 doi:10.20944/preprints202103.0206.v1

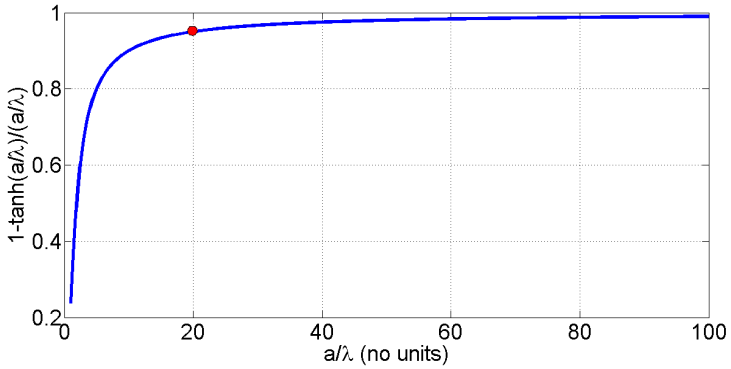

Figure 3. The variation of $\left[1-\frac{\lambda}{a}\tanh(\frac{a}{\lambda})\right]$ with a/λ

where λ is the Debye length depending on properties of the fluid and not on properties of the solid surfaces [e.g., 36,94].

Combining Eq. (9), Eq. (26) and Eq. (27), one obtains

$$i_s(a) = -\frac{\epsilon_r\epsilon_o\zeta}{\eta}\frac{2wa}{\tau}\left[1-\frac{\lambda}{a}\tanh(\frac{a}{\lambda})\right]\frac{\Delta P}{L_0} \tag{28}$$

Under most environmental conditions, ionic strengths (i.e., a proxy for ionic concentration) in potable water are normally between 10^{-3} and 10^{-2} mol/L [95]. Reservoirs can be saturated with brine with much higher ionic concentrations. Therefore, the Debye length is typically less than 10 nm at 25°C [94]. In addition, typical characteristic size of pore and fracture aperture in geological media is tens of micrometer [e.g., 96]. Therefore, the Debye length is normally much smaller than the pore sizes (thin EDL assumption). As seen in Fig. 3, when a is 20 times larger than λ, $1-\frac{\lambda}{a}\tanh(\frac{a}{\lambda})$ can be approximated as 1 with around 5% difference (see the red dot in Fig. 3). Under that condition, Eq. (28) is simplified to

$$i_s(w) = -\frac{\epsilon_r\epsilon_o\zeta}{\eta}\frac{2wa}{\tau}\frac{\Delta P}{L_0} = -\frac{\epsilon_r\epsilon_o\zeta}{\eta}\frac{2\beta w^2}{\tau}\frac{\Delta P}{L_0}. \tag{29}$$

Therefore, the total streaming current through the REV is given by [e.g., 53,56]

$$I_s = \int_{w_{min}}^{w_{max}} i_s(w)(-dN) \tag{30}$$

Combining Eq. (5), Eq. (29) and Eq. (30) yields

$$I_s = -\frac{2\epsilon_r\epsilon_o\zeta}{\eta\tau}\frac{\Delta P}{L_0}(\beta D_f w_{max}^{D_f})\int_{w_{min}}^{w_{max}} w^{1-D_f}dw = -\frac{2\epsilon_r\epsilon_o\zeta\beta D_f}{\eta\tau}\frac{w_{max}^2}{(2-D_f)}(1-\alpha^{2-D_f})\frac{\Delta P}{L_0}, \tag{31}$$

recall that $\alpha = w_{min}/w_{max}$.

3.4.2. Conduction current in the REV

The streaming current is responsible for the streaming potential ΔV that is set up across porous media under a fluid flow. This streaming potential will generate an electric conduction current that is opposite in direction with the streaming current. According to Ohm's law, the electrical conduction current density is given by

$$J_c = \sigma\frac{\Delta V}{L_o}, \tag{32}$$

Preprints (www.preprints.org) | NOT PEER-REVIEWED | Posted: 5 March 2021 doi:10.20944/preprints202103.0206.v1

recall that σ is the electrical conductivity of the REV that has been previously presented. Therefore, the total electrical conduction current through the REV is given by

$$I_c = J_c A_{REV}. \tag{33}$$

Combining Eq. (21), Eq. (32) and Eq. (33), the following is obtained

$$I_c = \frac{2\beta D_f w_{max}^2 (1-\alpha^{2-D_f})}{(2-D_f)\tau} \left\{ \sigma_w + \frac{(1+2\beta)\Sigma_s}{\beta w_{max}} \frac{2-D_f}{1-D_f} \frac{1-\alpha^{1-D_f}}{1-\alpha^{2-D_f}} \right\} \frac{\Delta V}{L_o}. \tag{34}$$

3.4.3. Streaming potential coupling coefficient

At steady state, the total electrical current through the REV is zero and one obtains

$$I_s + I_c = 0. \tag{35}$$

Combining Eq. (31), Eq. (34) and Eq. (35) yields

$$\Delta V = \frac{\epsilon_r \epsilon_0 \zeta \Delta P}{\eta \left[\sigma_w + \frac{(1+2\beta)\Sigma_s}{\beta w_{max}} \frac{2-D_f}{1-D_f} \frac{1-\alpha^{1-D_f}}{1-\alpha^{2-D_f}} \right]}. \tag{36}$$

Consequently, the SPCC is obtained as

$$C_S = \frac{\Delta V}{\Delta P} = \frac{\epsilon_r \epsilon_0 \zeta}{\eta \left[\sigma_w + \frac{(1+2\beta)\Sigma_s}{\beta w_{max}} \frac{2-D_f}{1-D_f} \frac{1-\alpha^{1-D_f}}{1-\alpha^{2-D_f}} \right]}. \tag{37}$$

Eq. (37) indicates that the SPCC for fractured media under fully saturated conditions is related to the zeta potential, fluid properties, specific surface conductance at the solid water interface and microstructural properties of the media (D_f, α, w_{max} and β). When Σ_s = 0, Eq. (37) reduces to the HS equation as shown by Eq. (2). It is indicated that for the negligible surface conductivity, the SPCC is independent of fracture size distribution and geometrically shaped pore structures.

Comparing Eq. (3) and Eq. (37), the characteristic length scale Λ (m) is obtained for fractured media as

$$\Lambda = w_{max} \frac{2\beta(1-D_f)(1-\alpha^{2-D_f})}{(1+2\beta)(2-D_f)(1-\alpha^{1-D_f})}. \tag{38}$$

It should be noted that Thanh et al. (2020) [56] and Rembert et al. (2020) [97] also obtained expressions for the characteristic length scale in porous media.

3.5. Effective excess charge density

Following the formalism presented by [52] or [54], we determine the effective excess charge density $\widehat{Q}_v$ (C/m^3) carried by the water flow in the REV. The effective excess charge density $\widehat{Q}_v^w$ (C/m^3) carried by the water flow in a single fracture with the width of w and aperture of 2a is defined by [e.g., 50,52,54]:

$$\widehat{Q}_v^w = \frac{1}{v_{av}(2aw)} \int_{-a}^{+a} \bar{Q}_v(y) v(y) (w.dy), \tag{39}$$

recall that $v(y)$, v_{av} and $\bar{Q}_v(y)$ is the velocity profile, the average velocity and the charge distribution in the fracture, respectively. Their expressions are presented in Eq. (9), Eq. (10) and Eq. (27), respectively. Combining Eq. (9), Eq. (10), Eq. (27) and Eq. (39), one obtains

$$\widehat{Q}_v^w = -\frac{3\epsilon_r \epsilon_o \zeta}{\beta^2 w^2} \left[1 - \frac{\lambda}{a} \tanh\left(\frac{a}{\lambda}\right) \right] \tag{40}$$

Preprints (www.preprints.org) | NOT PEER-REVIEWED | Posted: 5 March 2021 doi:10.20944/preprints202103.0206.v1

Under a thin EDL condition, Eq. (40) may be simplified as

$$\widehat{Q}_v^w = -\frac{3\epsilon_r\epsilon_o\zeta}{\beta^2 w^2}. \tag{41}$$

The effective excess charge $\widehat{Q}_v$ (C/m^3) carried by the water flow in the REV is defined by [e.g., 50,52]:

$$\begin{aligned}\widehat{Q}_v =& \frac{1}{v_D A_{REV}} \int_{w_{min}}^{w_{max}} \widehat{Q}_v^w v_{av}(2aw)(-dN) \\ =& -\frac{1}{v_D A_{REV}} \frac{2\epsilon_r\epsilon_o\zeta\beta D_f w_{max}^2}{\eta\tau} \frac{(1-\alpha^{2-D_f})}{2-D_f} \frac{\Delta P}{L_o},\end{aligned} \tag{42}$$

where A_{REV} is the cross-section area of the REV perpendicular to the flow direction and v_D is the Darcy's velocity (m/s) that is given by

$$v_D = \frac{k}{\eta}\frac{\Delta P}{L_o}, \tag{43}$$

recall that k is the permeability of porous media.

Combining Eq. (42) and Eq. (43), the following is obtained:

$$\widehat{Q}_v = -\frac{2\epsilon_r\epsilon_o\zeta\beta D_f w_{max}^2}{\tau k A_{REV}} \frac{(1-\alpha^{2-D_f})}{2-D_f}. \tag{44}$$

Substituting A_{REV} from Eq. (8) into Eq. (44), $\widehat{Q}_v$ in the REV is written as

$$\widehat{Q}_v = -\epsilon_r\epsilon_o\zeta\frac{\phi}{\tau^2 k}. \tag{45}$$

Eq. (45) shows the relationship between $\widehat{Q}_v$, macroscopic hydraulic parameters of porous media (the permeability, porosity, tortuosity) and electrokinetic parameters (the zeta potential). It is seen that the fracture size distribution and geometrically shaped fracture structures (w_{max}, α and β) do not directly appear in the closed-form equation for $\widehat{Q}_v$ as reported in literature [e.g., 52,95]. Note that Eq. (45) shows a behavior that is completely consistent with the empirical relationship proposed by [19]. To obtain the dependence of $\widehat{Q}_v$ on the parameters of w_{max}, α and β, we combine Eq. (15) and Eq. (45) to get the following:

$$\widehat{Q}_v = -\epsilon_r\epsilon_o\zeta\frac{3(4-D_f)(1-\alpha^{2-D_f})}{\beta^2 w_{max}^2(2-D_f)(1-\alpha^{4-D_f})}. \tag{46}$$

Comparing Eq. (21), Eq. (37) and Eq. (44), the relationship between the streaming potential coupling coefficient and effective charge density is obtained as

$$C_S = -\frac{k\widehat{Q}_v}{\eta\sigma}. \tag{47}$$

Eq. (47) is the same as Eq. (4) that has been developed for porous media using the volume averaging procedure [e.g., 43,98]. However, Eq. (47) is here explicitly developed from the assumptions made for fractured media. This confirms the findings of [47], [48] and [95], the coupling coefficient dependence to the pore space geometry (pore size distribution and pore shapes) can be taken into account in the effective excess charge density $\widehat{Q}_v$.

4. Results and discussion

Figure 4 shows the variation of the permeability of fractured media k with the fracture

Preprints (www.preprints.org) | NOT PEER-REVIEWED | Posted: 5 March 2021 doi:10.20944/preprints202103.0206.v1

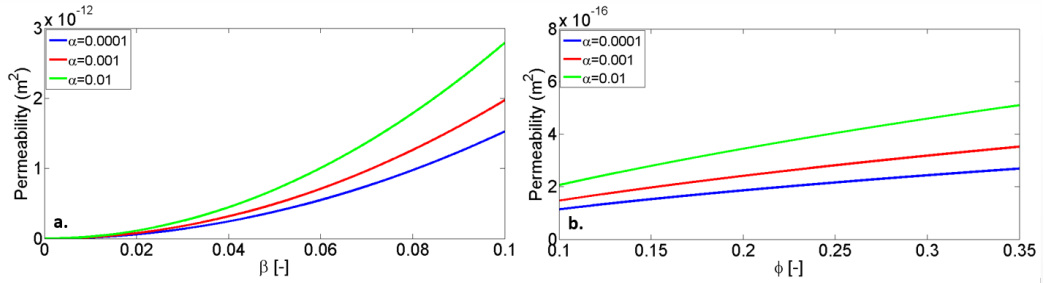

Figure 4. The variation of the permeability of fractured media k with the fracture aspect ratio β and porosity ϕ predicted from Eq. (15) for three values of α (0.0001, 0.001 and 0.01) with representative values of $w_{max} = 200.10^{-6}$ m, $\tau = 1.2$: (a) ϕ is fixed at 0.15; (b) β is fixed at 0.001.

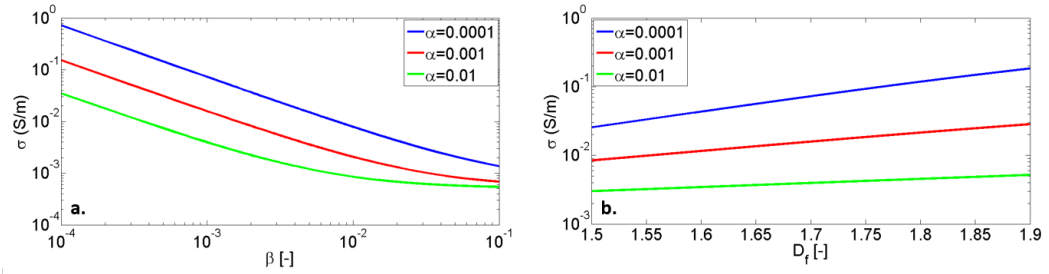

Figure 5. The variation of σ with the fracture aspect ratio β and the fractal dimension of the fracture sizes D_f predicted from Eq. (25) for three values of α (0.0001, 0.001 and 0.01) with representative values of $\sigma_w = 5.10^{-2}$ S/m, $\Sigma_s = 1.10^{-9}$ S, $F = 20$ and $w_{max} = 200.10^{-6}$ m. (a) D_f is fixed at 1.7. (b) β is fixed at 0.001.

aspect ratio β and porosity ϕ predicted from Eq. (15) for three values of the ratio of minimum to maximum apertures α (0.0001, 0.001 and 0.01) with representative values of $w_{max} = 200.10^{-6}$ m, $\tau = 1.2$: (a) ϕ is fixed at 0.15 and (b) β is fixed at 0.001. Note that we determine D_f from ϕ and α using Eq. (6). It is seen that the permeability increases with an increase of ϕ as reported in literature for fractured rocks [e.g., 75,99–101]. It can be explained by the fact that larger porosity means larger space occupied by fractures leading to larger permeability. Additionally, Fig. 4 also shows that the permeability increases with an increase of β and α. The reason for the increase of k with an increase of β may be that larger the fracture aspect ratio leads to higher flow rate and therefore higher permeability. The increase of k with an increase of α can be explained by the increase of the average fracture aperture with α as shown by [75].

Figure 5 shows the variation of the electrical conductivity of fractured media σ with the fracture aspect ratio β and the fractal dimension of the fracture sizes D_f for three values of α (0.0001, 0.001 and 0.01) with representative values of $\sigma_w = 10^{-2}$ S/m, $\Sigma_s = 1.5 \times 10^{-9}$ S, $F = 20$ and $w_{max} = 200.10^{-6}$ m: (a) D_f is fixed at 1.7 and (b) β is fixed at 0.001. It is seen that the σ is very sensitive with β, D_f and α. For given values of D_f and α, σ decreases with an increase of β. It can be explained by the decrease of the surface conductivity when β increases. Additionally, σ increases with an increase of D_f and with a decrease of α. That can be explained by an increase of the total number of fractures in the REV and therefore, the increase of surface conductivity with the increase of D_f and with the decrease of α (e.g., see [75] for more details).

Figure 6 predicts the variation of the SPCC with the fracture aspect ratio β and the maximum width w_{max} predicted from Eq. (37) for three values of α (0.0001, 0.001 and 0.01) with representative values of $\sigma_w = 2.10^{-2}$ S/m, $\Sigma_s = 1.10^{-9}$ S, ζ = -30 mV, $\phi = 0.15$: (a) w_{max} is fixed at 200.10^{-6} m and (b) β is fixed at 0.001. Similarly to previously mentioned, the value of D_f is determined from Eq. (6) with the knowledge of ϕ and α. It is seen that the SPCC in magnitude increases with an increase of β for a given value of α. Additionally, one can see that when α increases, the SPCC also increases. The reason is that σ decreases with

Preprints (www.preprints.org) | NOT PEER-REVIEWED | Posted: 5 March 2021 doi:10.20944/preprints202103.0206.v1

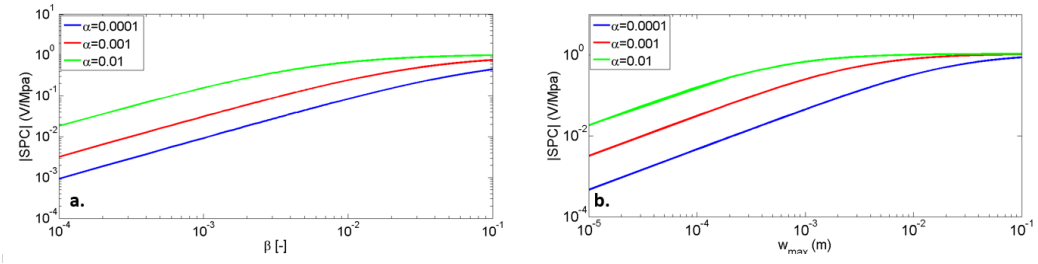

Figure 6. The variation of the SPCC with the fracture aspect ratio β and the maximum width w_{max} predicted from Eq. (37) for three values of α (0.0001, 0.001 and 0.01) with representative values of σ_w = 2.10^{-2} S/m, Σ_s = 1.10^{-9} S, ζ = -30 mV, ϕ = 0.15: (a) w_{max} is fixed at 200.10^{-6} m and (b) β is fixed at 0.001.

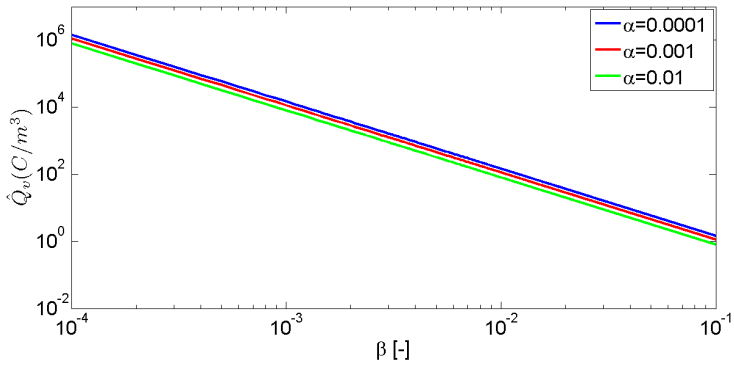

Figure 7. The variation of the $\widehat{Q}_v$ with the fracture aspect ratio β predicted from Eq. (46) for three values of α (0.0001, 0.001 and 0.01).

an increase of β and with increase of α. As deduced from Eq. (25) and Eq. (37), when σ decreases then the SPCC increases. The prediction also shows that the SPCC increases with an increase of w_{max}. This may be attributed to the fact that a larger fracture size leads to a lower surface electrical conductivity and therefore an increase of the SPCC. When w_{max} exceeds a certain value, the SPCC becomes independent of fracture sizes. The reason is that the surface electrical conductivity can be negligible at large fracture sizes as indicated by Eq. (22).

Figure 7 shows the variation of the $\widehat{Q}_v$ with the fracture aspect ratio β predicted from Eq. (46) for three values of α (0.0001, 0.001 and 0.01) with representative values of σ_w = 2.10^{-2} S/m, Σ_s = 1.10^{-9} S, ζ = -30 mV, ϕ = 0.15 and w_{max} = 200.10^{-6} m. It is seen that the $\widehat{Q}_v$ decreases with an increase of β and increase of α. As shown in Fig. 4 the permeability k increases with increasing β or α. That is in good match with results reported in [19] or [102] in which the $\widehat{Q}_v$ decreases with an increase of permeability k for porous media.

Due to lack of experimental data for fractured media, the model result is only compared with the experimental data published by [103] for three fractured limestones from different depths (samples A, B and C). The permeability, porosity and maximum width of fractured samples A, B and C are reported to be 1×10^{-17} m^2, 0.007, 80 μm; 4.69×10^{-16} m^2, 0.0107, 200 μm and 4.8×10^{-17} m^2, 0.006, 150 μm, respectively. Fig. 8 shows the comparison between the model result from Eq. (16) with the measured data for samples A, B and C. For the comparison, the model parameters β, τ and D_f are determined by seeking a minimum root-mean-square error (RMSE) through the "fminsearch" function in the MATLAB. We found β = 0.009, τ = 1.5 and D_f = 1.8 to give the minimum RMSE for fractured samples. Note that Ghanbarian et al. (2019) found the values of β between 0.1 and 0.001 by fitting their model to experimental data of tensile fractures in the Krafla fissure swarm of northeast Iceland [77]. Besides the 1:1 line (the solid line), the 1:10 and the 10:1 lines are also shown in Fig. 8 (the dashed lines). It is seen that the model predicts well the experimental data within

Preprints (www.preprints.org) | NOT PEER-REVIEWED | Posted: 5 March 2021 doi:10.20944/preprints202103.0206.v1

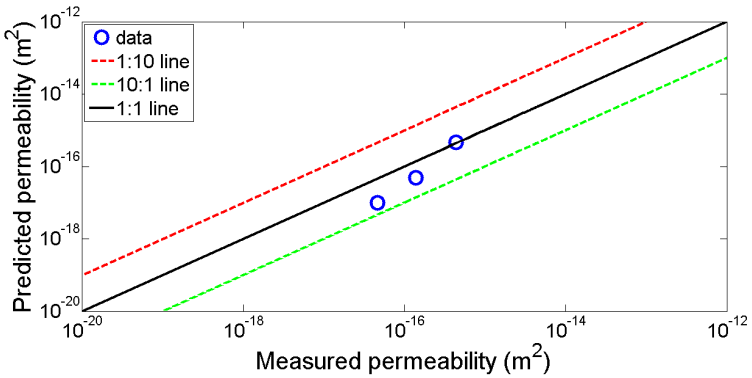

Figure 8. Comparison between measured permeability and calculated one for three fractured limestone samples obtained from [103] using Eq. (16).

less than 1 order of magnitude. Nevertheless, additional experimental laboratory studies or well controlled field measurements should be conducted to test our model further.

5. Conclusions

In this work, we conceptualize porous media as a bunch of parallel capillary fractures following a fractal pore size distribution to obtain the model for both electrical conductivity and SPCC. The later is expressed in terms of both the zeta potential and the effective charge density. We also propose an analytical model originating from the effective charge density approach that depends on macroscopic hydraulic and electrokinetic parameters of porous media. This work shows that when the surface electrical conductivity can be neglected, the proposed models reduces to ones obtained by a volume averaging procedure or a cylindrical capillary bundle model. It means that, in saturated conditions, the proposed models do not depend on the pore size distribution and geometrically shaped pore structures (w_{max}, α and β). We believe that the models proposed in this work can open-up new possibilities to study and monitor water flow in fractured media.

Acknowledgments

This research is funded by Vietnam National Foundation for Science and Technology Development (NAFOSTED) under grant number 103.99-2019.316

References

1. Revil, A.; Karaoulis, M.; Johnson, T.; Kemna, A. Review: Some low-frequency electrical methods for subsurface characterization and monitoring in hydrogeology. *Hydrogeology Journal* **2012**, *20*, 617–658. doi:10.1007/s10040-011-0819-x.
2. Binley, A.; Hubbard, S.S.; Huisman, J.A.; Revil, A.; Robinson, D.A.; Singha, K.; Slater, L.D. The emergence of hydrogeophysics for improved understanding of subsurface processes over multiple scales. *Water Resources Research* **2015**, *51*, 3837–3866. doi: https://doi.org/10.1002/2015WR017016.
3. Parsekian, A.D.; Singha, K.; Minsley, B.J.; Holbrook, W.S.; Slater, L. Multiscale geophysical imaging of the critical zone. *Reviews of Geophysics* **2015**, *53*, 1–26. doi: https://doi.org/10.1002/2014RG000465.
4. Jouniaux, L.; Pozzi, J.; Berthier, J.; Masse', P. Detection of fluid flow variations at the Nankai Trough by electric and magnetic measurements in boreholes or at the seafloor. *Journal of Geophysical Research* **1999**, *104*, 29293–29309.
5. Fagerlund, F.; Heinson, G. Detecting subsurface groundwater flow infractured rock using self-potential (SP) methods. *Environmental Geology* **2003**, *43*.
6. Titov, K.; Revil, A.; Konosavsky, P.; Straface, S.; Troisi, S. Numerical modelling of self-potential signals associated with a pumping test experiment. *Geophysical Journal International* **2005**, *162*, 641–650.

Preprints (www.preprints.org) | NOT PEER-REVIEWED | Posted: 5 March 2021 doi:10.20944/preprints202103.0206.v1

7. Aizawa, K.; Ogawa, Y.; Ishido, T. Groundwater flow and hydrothermal systems within volcanic edifices: Delineation by electric self-potential and magnetotellurics. *Journal of Geophysical Research* **2009**, *114*.
8. Singha, K.; Gorelick, S.M. Saline tracer visualized with three-dimensional electrical resistivity tomography: Field-scale spatial moment analysis. *Water Resources Research* **2005**, *41*. doi: https://doi.org/10.1029/2004WR003460.
9. Daily, W.; Ramirez, A.; LaBrecque, D.; Nitao, J. Electrical resistivity tomography of vadose water movement. *Water Resources Research* **1992**, *28*, 1429–1442. doi:https://doi.org/10.1029/91WR03087.
10. Finizola, A.; Lenat, N.; Macedo, O.; Ramos, D.; Thouret, J.; Sortino, F. Fluid circulation and structural discontinuities inside misti volcano (peru) inferred from sel-potential measurements. *Journal of Volcanology and Geothermal Research* **2004**, *135*, 343–360.
11. Mauri, G.; Williams-Jones, G.; Saracco, G. Depth determinations of shallow hydrothermal systems by self-potential and multi-scale wavelet tomography. *Journal of Volcanology and Geothermal Research* **2010**, *191*, 233–244.
12. Soueid Ahmed, A.; Revil, A.; Byrdina, S.; Coperey, A.; Gailler, L.; Grobbe, N.; Viveiros, F.; Silva, C.; Jougnot, D.; Ghorbani, A.; Hogg, C.; Kiyan, D.; Rath, V.; Heap, M.J.; Grandis, H.; Humaida, H. 3D electrical conductivity tomography of volcanoes. *Journal of Volcanology and Geothermal Research* **2018**, *356*, 243–263. doi:10.1016/j.jvolgeores.2018.03.017.
13. Martinez-Pagan, P.; Jardani, A.; Revil, A.; Haas, A. Self-potential monitoring of a salt plume. *Geophysics* **2010**, *75*, WA17–WA25. doi:10.1190/1.3475533.
14. Naudet, V.; Revil, A.; Bottero, J.Y.; Bégassat, P. Relationship between self-potential (SP) signals and redox conditions in contaminated groundwater. *Geophysical Research Letters* **2003**, *30*. doi: 10.1029/2003GL018096.
15. Doussan, C.; Jouniaux, L.; Thony, J.L. Variations of self-potential and unsaturated water flow with time in sandy loam and clay loam soils. *Journal of Hydrology* **2002**, *267*, 173 – 185.
16. Jougnot, D.; Linde, N.; Haarder, E.; Looms, M. Monitoring of saline tracer movement with vertically distributed self-potential measurements at the HOBE agricultural test site, Voulund, Denmark. *Journal of Hydrology* **2015**, *521*, 314 – 327.
17. Mares, R.; Barnard, H.R.; Mao, D.; Revil, A.; Singha, K. Examining diel patterns of soil and xylem moisture using electrical resistivity imaging. *Journal of Hydrology* **2016**, *536*, 327–338. doi: https://doi.org/10.1016/j.jhydrol.2016.03.003.
18. Voytek, E.B.; Barnard, H.R.; Jougnot, D.; Singha, K. Transpiration- and precipitation-induced subsurface water flow observed using the self-potential method. *Hydrological Processes* **2019**, *33*, 1784–1801.
19. Jardani, A.; Revil, A.; Boleve, A.; Crespy, A.; Dupont, J.P.; Barrash, W.; Malama, B. Tomography of the Darcy velocity from self-potential measurements. *Geophysical Research Letters* **2007**, *34*. doi:10.1029/2007GL031907.
20. Pollock, D.; Cirpka, O.A. Fully coupled hydrogeophysical inversion of synthetic salt tracer experiments. *Water Resources Research* **2010**, *46*.
21. Stesky, R.M. Electrical conductivity of brine-saturated fractured rock. *Geophysics* **1986**, *51*, 1585–1593. doi:10.1190/1.1442209.
22. Shen, J.; Su, B.; Guo, N. Anisotropic characteristics of electrical responses of fractured reservoir with multiple sets of fractures. *Petroleum Science* **2009**, *6*, 127–138. doi:10.1007/s12182-009-0021-0.
23. Roubinet, D.; Irving, J. Discrete-dual-porosity model for electric current flow in fractured rock. *Journal of Geophysical Research: Solid Earth* **2014**, *119*, 767–786.
24. Wishart, D.N.; Slater, L.D.; Gates, A.E. Self potential improves characterization of hydraulically-active fractures from azimuthal geoelectrical measurements. *Geophysical Research Letters* **2006**, *33*, L17314.
25. Maineult, A.; Thomas, B.; Nussbaum, C.; Wieczorek, K.; Gibert, D.; Lavielle, B.; Kergosien, B.; Nicollin, F.; Mahiouz, K.; Lesparre, N. Anomalies of noble gases and self-potential associated with fractures and fluid dynamics in a horizontal borehole, Mont Terri Underground Rock Laboratory. *Engineering Geology* **2013**, *156*, 46 – 57.
26. Berkowitz, B. Characterizing flow and transport in fractured geological media: A review. *Advances in Water Resources* **2002**, *25*, 861–884. doi:https://doi.org/10.1016/S0309-1708(02)00042-8.
27. Gélis, C.; Revil, A.; Cushing, M.E.; Jougnot, D.; Lemeille, F.; Cabrera, J.; de Hoyos, A.; Rocher, M. Potential of Electrical Resistivity Tomography to Detect Fault Zones in Limestone and Argillaceous Formations in the Experimental Platform of Tournemire, France. *Pure and Applied Geophysics* **2010**, *167*, 1405–1418. doi:10.1007/s00024-010-0097-x.

Preprints (www.preprints.org) | NOT PEER-REVIEWED | Posted: 5 March 2021 doi:10.20944/preprints202103.0206.v1

28. Lesparre, N.; Boyle, A.; Grychtol, B.; Cabrera, J.; Marteau, J.; Adler, A. Electrical resistivity imaging in transmission between surface and underground tunnel for fault characterization. *Journal of Applied Geophysics* **2016**, *128*, 163–178. doi:https://doi.org/10.1016/j.jappgeo.2016.03.004.
29. Haas, A.K.; Revil, A.; Karaoulis, M.; Frash, L.; Hampton, J.; Gutierrez, M.; Mooney, M. Electric potential source localization reveals a borehole leak during hydraulic fracturing. *GEOPHYSICS* **2013**, *78*, D93–D113. doi:10.1190/geo2012-0388.1.
30. DesRoches, A.J.; Butler, K.E.; MacQuarrie, K.T. Surface self-potential patterns related to transmissive fracture trends during a water injection test. *Geophysical Journal International* **2018**, *212*, 2047–2060.
31. Demirel, S.; Roubinet, D.; Irving, J.; Voytek, E. Characterizing Near-Surface Fractured-Rock Aquifers: Insights Provided by the Numerical Analysis of Electrical Resistivity Experiments. *Water* **2018**, *10*, 1117. doi:10.3390/w10091117.
32. Bernabe, Y. The transport properties of networks of cracks and pores. *Journal of Geophysical Research: Solid Earth* **1995**, *100*, 4231–4241. doi:https://doi.org/10.1029/94JB02986.
33. Roubinet, D.; Irving, J.; Pezard, P. Relating Topological and Electrical Properties of Fractured Porous Media: Insights into the Characterization of Rock Fracturing. *Minerals* **2018**, *8*, 14. doi:10.3390/min8010014.
34. Archie, G.E. The electrical resistivity log as an aid in determining some reservoir characteristics. *Petroleum Transactions of AIME* **1942**, *146*, 54–62.
35. Overbeek, J. *Electrochemistry of the double layer: in Colloid Science, Irreversible Systems, H. R. Kruyt, Ed.*; Elsevier, 1952.
36. Hunter, R.J. *Zeta Potential in Colloid Science*; Academic, New York, 1981.
37. Pride, S. Governing equations for the coupled electromagnetics and acoustics of porous media. *Physical Review B* **1994**, *50*, 15678–15696.
38. Bernabé, Y. Streaming potential in heterogeneous networks. *Journal of Geophysical Research: Solid Earth* **1998**, *103*, 20827–20841.
39. Morgan, F.D.; Williams, E.R.; Madden, T.R. Streaming potential properties of westerly granite with applications. *Journal of Geophysical Research* **1989**, *94*, 12.449–12.461.
40. Revil, A.; Pezard, P.A.; Glover, P.W.J. Streaming potential in porous media 1. Theory of the zeta potential. *Journal of Geophysical Research* **1999**, *104*, 20021–20031.
41. Glover, P.W.J.; Dery, N. Streaming potential coupling coefficient of quartz glass bead packs: Dependence on grain diameter, pore size, and pore throat radius. *Geophysics* **2010**, *75*, F225–F241.
42. Kormiltsev, V.V.; Ratushnyak, A.N.; Shapiro, V.A. Three-dimensional modeling of electric and magnetic fields induced by the fluid flow movement in porous media. *Physics of the Earth and Planetary Interiors* **1998**, *105*, 109 – 118.
43. Revil, A.; Leroy, P. Constitutive equations for ionic transport in porous shales. *Journal of Geophysical Research: Solid Earth* **2004**, *109*. B03208, doi:10.1029/2003JB002755.
44. Jougnot, D.; Roubinet, D.; Guarracino, L.; Maineult, A. *Modeling Streaming Potential in Porous and Fractured Media, Description and Benefits of the Effective Excess Charge Density Approach*; In: Biswas A., Sharma S. (eds) Advances in Modeling and Interpretation in Near Surface Geophysics. Springer Geophysics. Springer, Cham, 2020.
45. Ishido, T.; Mizutani, H. Experimental and Theoretical Basis of Electrokinetic Phenomena in Rock-Water Systems and Its Applications to Geophysics. *Journal of Geophysical Research* **1981**, *86*, 1763–1775.
46. Jackson, M.D. Characterization of multiphase electrokinetic coupling using a bundle of capillary tubes model. *Journal of Geophysical Research: Solid Earth* **2008**, *113*. B04201, doi:10.1029/2007JB005490.
47. Linde, N. Comment on "Characterization of multiphase electrokinetic coupling using a bundle of capillary tubes model" by Mathew D. Jackson. *Journal of Geophysical Research: Solid Earth* **2009**, *114*. B06209, doi:10.1029/2008JB005845.
48. Jackson, M.D. Multiphase electrokinetic coupling: Insights into the impact of fluid and charge distribution at the pore scale from a bundle of capillary tubes model. *Journal of Geophysical Research: Solid Earth* **2010**, *115*. B07206, doi:10.1029/2009JB007092.
49. Revil, A.; Woodruff, W.F.; Lu, N. Constitutive equations for coupled flows in clay materials. *Water Resources Research* **2011**, *47*. W05548, doi:10.1029/2010WR010002.
50. Jougnot, D.; Linde, N.; Revil, A.; Doussan, C. Derivation of soil-specific streaming potential electrical parameters from hydrodynamic characteristics of partially saturated soils. *Vadose Zone Journal* **2012**, *11*, 272–286.

Preprints (www.preprints.org) | NOT PEER-REVIEWED | Posted: 5 March 2021 doi:10.20944/preprints202103.0206.v1

51. Jackson, M.; Leinov, E. On the Validity of the "Thin" and "Thick" Double-Layer Assumptions When Calculating Streaming Currents in Porous Media. *International Journal of Geophysics* **2012**, *2012*.
52. Guarracino, L.; Jougnot, D. A Physically Based Analytical Model to Describe Effective Excess Charge for Streaming Potential Generation in Water Saturated Porous Media. *Journal of Geophysical Research: Solid Earth* **2018**, *123*, 52–65.
53. Thanh, L.D.; Van Do, P.; Van Nghia, N.; Ca, N.X. A fractal model for streaming potential coefficient in porous media. *Geophysical Prospecting* **2018**, *66*, 753–766.
54. Soldi, M.; Guarracino, L.; Jougnot, D. An analytical effective excess charge density model to predict the streaming potential generated by unsaturated flow. *Geophysical Journal International* **2019**, *216*, 380–394.
55. Soldi, M.; Guarracino, L.; Jougnot, D. An effective excess charge model to describe hysteresis effects on streaming potential. *Journal of Hydrology* **2020**, p. 124949.
56. Thanh, L.; Jougnot, D.; Do, P.; Ca, N.; Hien, N. A Physically Based Model for the Streaming Potential Coupling Coefficient in Partially Saturated Porous Media. *Water* **2020**, *12*, 1588.
57. Shi, P.; Guan, W.; Hu, H. Dependence of Dynamic Electrokinetic-Coupling-Coefficient on the Electric Double Layer Thickness of fluid-filled porous formations. *Annals of Geophysics* **2018**, *61*, SE340.
58. Erickson, D.; Li, D. Analysis of Alternating Current Electroosmotic Flows in a Rectangular Microchannel. *Langmuir* **2003**, *19*, 5421–5430.
59. Wu, R.C.; Papadopoulos, K.D. Electroosmotic flow through porous media: cylindrical and annular models. *Colloids and Surfaces A: Physicochemical and Engineering Aspects* **2000**, *161*, 469 – 476.
60. Pascal, J.; Oyanader, M.; Arce, P. Effect of capillary geometry on predicting electroosmotic volumetric flowrates in porous or fibrous media. *Journal of Colloid and Interface Science* **2012**, *378*, 241 – 250.
61. Thanh, L.; Jougnot, D.; Do, P.; Mendieta, M.; Ca, N.; Hoa, V.X., T.P.; Hien, N. Electroosmotic coupling in porous media, a new model based on a fractal upscaling procedure. *Transport in Porous Media* **2020**, *134*, 249–274.
62. Nourbehecht, B. *Irreversible thermodynamic effects in inhomogeneous media and their applications in certain geoelectric problems*; PhD thesis, MIT Press, Cambridge, Mass, USA, 1963.
63. Smoluchowski, M. Contribution à la theorie de l'endosmose electrique et de quelques phenomènes correlatifs. *Bulletin international de l'Academie des Sciences de Cracovie* **1903**, *8*, 182 – 200.
64. Johnson, D.L.; Koplik, J.; Schwartz, L.M. New Pore-Size Parameter Characterizing Transport in Porous Media. *Phys. Rev. Lett.* **1986**, *57*, 2564–2567. doi:10.1103/PhysRevLett.57.2564.
65. Katz, A.J.; Thompson, A.H. Fractal Sandstone Pores: Implications for Conductivity and Pore Formation. *Phys. Rev. Lett.* **1985**, *54*, 1325–1328.
66. Bo-Ming, Y. Fractal Character for Tortuous Streamtubes in Porous Media. *Chinese Physics Letters* **2005**, *22*, 158.
67. Chelidze, T.; Gueguen, Y. Evidence of fractal fracture. *International Journal of Rock Mechanics and Mining Sciences Geomechanics Abstracts* **1990**, *27*, 223 – 225.
68. Watanabe, K.; Takahashi, H. Fractal geometry characterization of geothermal reservoir fracture networks. *Journal of Geophysical Research: Solid Earth* **1995**, *100*, 521–528.
69. Yu, B.; Cheng, P. A fractal permeability model for bi-dispersed porous media. *International Journal of Heat and Mass Transfer* **2002**, *45*, 2983–2993.
70. Roubinet, D.; Linde, N.; Jougnot, D.; Irving, J. Streaming potential modeling in fractured rock: Insights into the identification of hydraulically active fractures. *Geophysical Research Letters* **2016**, *43*, 4937–4944.
71. Tyler, S.W.; Wheatcraft, S.W. Fractal processes in soil water retention. *Water Resources Research* **1990**, *26*, 1047–1054.
72. Miao, T.; Yu, B.; Duan, Y.; Fang, Q. A fractal analysis of permeability for fractured rocks. *International Journal of Heat and Mass Transfer* **2015**, *81*, 75 – 80.
73. Wang, S.; Wu, T.; Cao, X.; Zheng, Q.; Ai, M. A fractal model for gas apparent permeability in microfractures of tight/shale reservoirs. *Fractals* **2017**, *25*, 1750036.
74. Majumdar, A.; Bhushan, B. Role of Fractal Geometry in Roughness Characterization and Contact Mechanics of Surfaces. *Journal of Tribology* **1990**, *112*, 205–216. doi:10.1115/1.2920243.
75. Deng, P.; Zhu, J. Equivalent Permeability of Fractured Media Incorporating Tortuosity and Nonlinear Flow. *Transport in Porous Media* **2020**, *132*, 741–760. doi:10.1007/s11242-020-01410-3.

Preprints (www.preprints.org) | NOT PEER-REVIEWED | Posted: 5 March 2021 doi:10.20944/preprints202103.0206.v1

76. Torabi, A.; Berg, S.S. Scaling of fault attributes: A review. *Marine and Petroleum Geology* **2011**, *28*, 1444 – 1460.
77. Ghanbarian, B.; Perfect, E.; Liu, H.H. A geometrical aperture-width relationship for rock fractures. *Fractals* **2019**, *27*, 1940002. doi:10.1142/S0218348X19400024.
78. Scheidegger, A.E. The Physics of Flow Through Porous Media. *Soil Science* **1958**, *86*, 355.
79. Yu, B.; Liu, W. Fractal analysis of permeabilities for porous media. *AIChE Journal* **2004**, *50*, 46–57.
80. Thanh, L.D.; Jougnot, D.; Van Do, P.; Van Nghia A, N. A physically based model for the electrical conductivity of water-saturated porous media. *Geophysical Journal International* **2019**, *219*, 866–876.
81. Chung, C. *Extrusion of Polymers 2E: Theory and Practice*; Hanser Publications; 2nd edition, 2010.
82. Neuzil, C.E.; Tracy, J.V. Flow through fractures. *Water Resources Research* **1981**, *17*, 191–199. doi: 10.1029/WR017i001p00191.
83. Klimczak, C.; Schultz, R.; Parashar, R.; Reeves, D. Cubic law with aperture-length correlation: Implications for network scale fluid flow. *Hydrogeology Journal* **2010**, *18*, 851–862.
84. Pfannkuch, H.O. On the Correlation of Electrical Conductivity Properties of Porous Systems with Viscous Flow Transport Coefficients. *Developments in Soil Science* **1972**, *2*, 42 – 54.
85. Waxman, M.H.; Smits, L.J.M. Electrical conductivities in oil bearing shaly sands. *Society of Petroleum Engineers Journal* **1968**, *8*, 107–122.
86. Revil, A.; Cathles III, L.M.; Losh, S.; Nunn, J.A. Electrical conductivity in shaly sands with geophysical applications. *Journal of Geophysical Research: Solid Earth* **1998**, *103*, 23925–23936. doi: 10.1029/98JB02125.
87. Friedman, S.P. Soil properties influencing apparent electrical conductivity: a review. *Computers and Electronics in Agriculture* **2005**, *46*, 45 – 70. doi:https://doi.org/10.1016/j.compag.2004.11.001.
88. Linde, N.; Binley, A.; Tryggvason, A.; Pedersen, L.B.; Revil, A. Improved hydrogeophysical characterization using joint inversion of cross-hole electrical resistance and ground-penetrating radar traveltime data. *Water Resources Research* **2006**, *42*.
89. Glover, P. What is the cementation exponent? A new interpretation. *The Leading Edge* **2009**, *28*, 82–85.
90. Brovelli, A.; Cassiani, G. Combined estimation of effective electrical conductivity and permittivity for soil monitoring. *Water Resources Research* **2011**, *47*.
91. Rice, C.; Whitehead, R. Electrokinetic flow in a narrow cylindrical capillary. *J. Phys. Chem.* **1965**, *69*, 4017–4024.
92. Pride, S.R.; Morgan, F.D. Electrokinetic dissipation induced by seismic waves. *Geophysics* **1991**, *56*, 914–925.
93. Kirby, B.J.; Hasselbrink Jr., E.F. Zeta potential of microfluidic substrates: 1. Theory, experimental techniques, and effects on separations. *ELECTROPHORESIS* **2004**, *25*, 187–202.
94. Israelachvili, J. *Intermolecular and Surface Forces*; Academic Press, 1992.
95. Jougnot, D.; Mendieta, A.; Leroy, P.; Maineult, A. Exploring the Effect of the Pore Size Distribution on the Streaming Potential Generation in Saturated Porous Media, Insight From Pore Network Simulations. *Journal of Geophysical Research: Solid Earth* **2019**, *124*, 5315–5335.
96. Hu, X.; Hu, S.; Jin, F.; Huang, S. *Physics of Petroleum Reservoirs*; Springer-Verlag Berlin Heidelberg, 2017.
97. Rembert, F.; Jougnot, D.; Guarracino, L. A fractal model for the electrical conductivity of water-saturated porous media during mineral precipitation-dissolution processes. *Advances in Water Resources* **2020**, *145*, 103742. doi:https://doi.org/10.1016/j.advwatres.2020.103742.
98. Revil, A.; Linde, N.; Cerepi, A.; Jougnot, D.; Matthäi, S.; Finsterle, S. Electrokinetic coupling in unsaturated porous media. *Journal of Colloid and Interface Science* **2007**, *313*, 315 – 327.
99. Tiab, D.; Donaldson, E.C. Chapter 3 - Porosity and Permeability. In *Petrophysics*, Fourth Edition ed.; Tiab, D.; Donaldson, E.C., Eds.; Gulf Professional Publishing: Boston, 2016; pp. 67 – 186.
100. Erol, S.; Fowler, S.; Harcouët-Menou, V.; Laenen, B. An Analytical Model of PorosityPermeability for Porous and Fractured Media. *Transport in Porous Media* **2017**, *120*, 327–358.
101. Lamur, A.; Kendrick, J.; Eggertsson, G.; Wall, R.; Ashworth, J.; Lavallée, Y. The permeability of fractured rocks in pressurised volcanic and geothermal systems. *Scientific Reports* **2017**, *7*. doi: 10.1038/s41598-017-05460-4.
102. Cherubini, A.; Garcia, B.; Cerepi, A.; Revil, A. Streaming Potential Coupling Coefficient and Transport Properties of Unsaturated Carbonate Rocks. *Vadose Zone Journal* **2018**, *17*, 180030.
103. Chilingarian, G.; Mazzullo, S.; Rieke, H. *Carbonate reservoir characterization: a geologic-engineering analysis, part I.*; Elsevier Science, 1992.

Preprints (www.preprints.org) | NOT PEER-REVIEWED | Posted: 5 March 2021 doi:10.20944/preprints202103.0206.v1